

Single-Source Multiaxis Cold-Atom Interferometer in a Centimeter-Scale Cell

Yun-Jhih Chen,^{1,2,*} Azure Hansen,¹ Gregory W. Hoth,^{1,2,†} Eugene Ivanov,^{1,3} Bruno Pelle,^{1,2,‡}
John Kitching,¹ and Elizabeth A. Donley¹

¹*National Institute of Standards and Technology, Boulder, Colorado 80305, USA*

²*University of Colorado, Boulder, Colorado 80309, USA*

³*University of Western Australia, Perth, Western Australia 6009, Australia*

 (Received 11 December 2018; revised manuscript received 20 May 2019; published 11 July 2019)

Using point-source atom interferometry (PSI), we characterize the sensitivity of a multiaxis gyroscope based on free-space Raman interrogation of a single source of cold atoms in a glass vacuum cell. The instrument simultaneously measures the acceleration in the direction of the Raman-laser beams and the projection of the rotation vector onto the plane perpendicular to that direction. The sensitivities for the magnitude and direction of the rotation-vector measurement are $0.033^\circ/\text{s}$ and 0.27° with an averaging time of 1 s, respectively. The fractional acceleration sensitivity $\delta g/g$ is $1.6 \times 10^{-5}/\sqrt{\text{Hz}}$. The sensitivity can be increased by increasing the Raman interrogation time, allowing the cold-atom cloud to expand further, correcting the fluctuations in the initial cloud shape, and reducing sources of technical noise. PSI resolves a rotation vector in a plane by measuring a phase gradient. This two-dimensional rotation sensitivity may be specifically important for applications such as tracking the precession of a rotation vector and gyrocompassing.

DOI: [10.1103/PhysRevApplied.12.014019](https://doi.org/10.1103/PhysRevApplied.12.014019)

I. INTRODUCTION

Light-pulse atom interferometers may help answer some of the most-important questions in fundamental physics [1–4] because of their extraordinary sensitivity to inertial effects [5–7]. They may also have applications in navigation and geodesy because of their long-term stability and accuracy [8–12]. The realization of atom interferometers of small size, low weight, and low power would facilitate their transition from the laboratory to applications in the field [13–17]. Several groups have demonstrated portable atom-interferometer gravimeters for field use [18–22].

Light-pulse-atom-interferometer gyroscopes are typically more complex than gravimeters. Multiple cold-atom sources or a four-pulse Raman geometry are often used to distinguish between interferometer phase shifts induced by rotation and by acceleration. The approach with multiple cold-atom sources has been demonstrated with counter-propagating atomic beams [8,23–25] and cold-atom clouds [9,26–31] using the most-common beamsplitter-mirror-beamsplitter Raman pulse sequence [32]. Since the rotational phase shifts depend on the atom velocity while the

acceleration phase shifts do not, the rotation and acceleration measurements are constructed from linear combinations of the signals from the counterpropagating cold-atom sources. This approach was successfully implemented in a compact package with a high data rate [29]. The approach with a four-pulse “butterfly” Raman geometry [9–12,33] was demonstrated with a single atom cloud. In this configuration, the rotational phase shift depends on the magnitude of the acceleration in the direction orthogonal to the rotation axis and the Raman beams, complicating the extraction of pure rotation in a sensor that is not geostationary [10]. Atom interferometers with the aforementioned three-pulse or four-pulse configuration measure one axis of rotation. Their multiaxis sensitivity can be achieved by interleaving measurements with Raman beams propagating along different axes and/or with different pulse sequences, as demonstrated in Refs. [9,33].

In most light-pulse-atom-interferometer techniques, the thermal expansion of the cold-atom cloud is unwanted because it reduces the fringe contrast. In contrast, point-source atom interferometry (PSI) utilizes the thermal expansion of the cold-atom cloud to map the velocity-dependent phase shifts onto an imaging plane. Thermal clouds have also been implemented in guided-wave atom interferometry for inertial sensing. In the work reported in Refs. [34,35], atoms were prepared in a low-magnetic-field-seeking state and loaded into a magnetic guide, and the manipulation of the matter wave was realized by

*yunjih.chen@colorado.edu

†Present address: Department of Physics, University of Strathclyde, Glasgow G4 0NG, United Kingdom.

‡Present address: MUQUANS, Institut d’Optique d’Aquitaine, rue François Mitterrand, 33400 Talence, France.

the scattering of the thermal cloud in the Kapitza-Dirac regime.

PSI is a simultaneous multi-axis-gyroscope technique based on a single source of atoms. PSI was demonstrated in a 10-m atomic fountain [36,37] designed to enable precision tests of the equivalence principle [38]. In PSI, the beamsplitter-mirror-beamsplitter Raman pulse sequence is applied to an isotropically expanding cloud of atoms in which each atom interferes only with itself. Because the enclosed area of the matter-wave Mach-Zehnder interferometer depends on the momentum kick applied to the atom and the atom velocity, the thermal velocity spread of the expanding cloud creates many Mach-Zehnder interferometers spanning all directions in a single operation. Each atom acts as an interferometer generating an interferometer phase that depends on the atom's initial velocity, as illustrated in Fig. 1. The strong position-velocity correlation for atoms in the expanded cloud preserves the phase shifts that are detected as an image. Spatial fringes arising from rotations are imprinted on the population distribution between the hyperfine ground states. From the fringe pattern, the acceleration in the propagation direction of the Raman-laser beams and the projection of the rotation vector onto the plane perpendicular to that direction are measured simultaneously.

Taking advantage of the dramatic simplifications provided by PSI, we have developed a process amenable to portable applications in which a single cloud of atoms expands and falls by only a few millimeters during an interrogation cycle. We previously demonstrated rotation measurements with PSI and characterized a systematic error due to the finite size of the cold-atom cloud [39]. Here we demonstrate the measurement of the acceleration in one direction and the rotation vector in the plane perpendicular

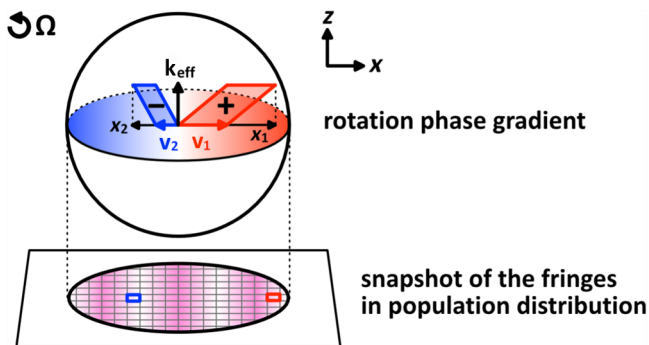


FIG. 1. Parallel operation of many Mach-Zehnder atom interferometers with a cloud of cold atoms expanding inside a pair of counterpropagating Raman-laser beams of relatively large beam diameter, oriented along z . Two of the many atom interferometers are shown, indicated in red and blue. The position-velocity correlation of a point source preserves the interferometer phase shifts, which are read out as an image of spatial fringes in a population distribution.

to that direction and we evaluate the sensitivity of the rotation-vector measurement.

II. SIMULTANEOUS MULTIAXIS INERTIAL SENSING WITH PSI

In a ballistically expanding cloud of cold atoms, if the final size of the cloud is much larger than the initial size, referred to as the “point-source approximation,” the position of an atom is related to its velocity \mathbf{v} and the expansion time T_{ex} of the cloud by $\mathbf{r} = \mathbf{v}T_{\text{ex}}$. In PSI, a beamsplitter-mirror-beamsplitter ($\pi/2$ - π - $\pi/2$) pulse sequence is applied to the cloud during its expansion. At the time the cloud is detected, the interferometer phase shift from inertial forces is mapped onto space with the leading terms as

$$\Phi(\mathbf{r}) = \mathbf{k}_{\text{eff}} \cdot \mathbf{a}T^2 + \mathbf{k}_{\Omega} \cdot \mathbf{r}. \quad (1)$$

The first term is the interferometer phase due to a homogeneous acceleration and the second term is a phase gradient across the cloud due to the rotation of the system. The phase gradient is $\mathbf{k}_{\Omega} = (\mathbf{k}_{\text{eff}} \times \boldsymbol{\Omega})2T^2/T_{\text{ex}}$, where \mathbf{k}_{eff} is the effective Raman transition wavevector, $\boldsymbol{\Omega}$ is the angular velocity of the system, and T is the time between Raman pulses.

Since the population ratio is a sinusoidal function of the interferometer phase, the phase gradient across the cloud induced by rotation leads to fringes in the population distribution. The contributions to the interferometer phase from the rotation components perpendicular to \mathbf{k}_{eff} and the acceleration in the direction of \mathbf{k}_{eff} are distinguishable because they modify the spatial-fringe pattern in the image plane in distinct and independent ways. The frequency of the fringes is proportional to the magnitude of the rotation projected onto the plane perpendicular to \mathbf{k}_{eff} . The orientation of the fringes indicates the direction of rotation projected onto that plane. The uniform acceleration translates the fringes spatially without affecting the period or the direction of the fringes because the acceleration shifts the overall phase but does not change the phase gradient.

In our experiment, as illustrated in Fig. 2, the Raman-laser beams propagate along the z axis and therefore the atoms sense the acceleration in the z direction and the components of rotation in the x - y plane. In the point-source approximation, all atoms with the same velocity components in the x - y plane have the same final (x, y) position and the same Sagnac area and thus the same interferometer phase shift. We image the cold-atom cloud in the x - y plane, which preserves the fringe contrast because signals with the same interferometer phase are integrated along z onto the same pixel in the image.

When the initial cloud size is not a point source, the rotation-fringe contrast and the number of fringes will be

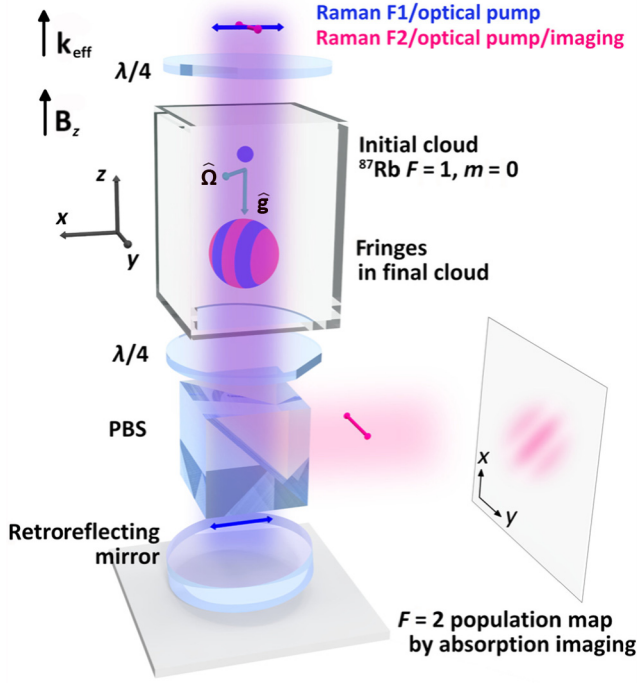


FIG. 2. The glass vacuum cell and surrounding optics of our PSI science package. The inner dimension of the glass cell is 1 cm². The instrument measures the acceleration in the z direction and the projection of the rotation vector onto the x - y plane. PBS, polarizing beam splitter.

lower than that of an ideal point source [39]. A finite-sized cold-atom cloud can be considered as a collection of many point sources. Mathematically, the fringe pattern will be the convolution of this initial cloud shape and the fringe pattern of a point source. As a result of the convolution, fringe contrast is reduced, the number of fringes is lower, and the direction of the fringes is modified by the initial cloud shape. In the special case where the cloud has a Gaussian distribution for both position and velocity, the x and y components of the phase gradient \mathbf{k}_Ω are reduced as [39]

$$\begin{aligned} k'_{\Omega,x} &= k_{\Omega,x}(1 - \sigma_{0x}^2/\sigma_{fx}^2), \\ k'_{\Omega,y} &= k_{\Omega,y}(1 - \sigma_{0y}^2/\sigma_{fy}^2), \end{aligned} \quad (2)$$

where $k_{\Omega,x} = -2k_{\text{eff}}T^2\Omega_y/T_{\text{ex}}$ and $k_{\Omega,y} = 2k_{\text{eff}}T^2\Omega_x/T_{\text{ex}}$ are the x and y components of the phase gradient for a point source, respectively. The expansion time T_{ex} is measured from the time when the cold-atom cloud is released from the magneto-optical trap (MOT) or molasses to the time when it is imaged. The terms σ_{0x} and σ_{0y} are the standard deviation of the initial Gaussian cloud in the x - y plane, and σ_{fx} and σ_{fy} are the standard deviations when the cloud is imaged.

III. PSI WITH COMPACT SCIENCE PACKAGE

Our PSI experiment uses laser-cooled ⁸⁷Rb atoms in a glass cell with 1-cm² cross-section area. A manifold that includes an ion pump, a Rb dispenser, and a vacuum window is connected to the glass cell. Figure 2 shows an illustration of our compact science package, including only the glass cell and the surrounding optics. In the glass cell, the laser beams for state preparation, Raman interrogation, and detection propagate vertically in a shared beam path with an e^{-2} beam diameter of 8 mm and are circularly polarized inside the glass cell. Three orthogonal and retroreflected beams (not shown in the figure) with e^{-2} diameters of 6 mm form the MOT for ⁸⁷Rb. The cooling and repumping laser powers are 5.6 and 1.3 mW in each beam, respectively. The laser system that generates the laser beams for the experiment is described in Appendix A.

Each experimental cycle starts with a ⁸⁷Rb MOT and optical molasses that prepare a cloud of about 10^7 atoms. The cloud temperature is about 6 μ K, and the standard deviation of the Gaussian initial cloud shape is 0.3 mm. The loading and cooling phases of each cycle are 85% of the total cycle when the experimental repetition rate is 5 Hz (and 70% at 10 Hz). We apply a 0.7-G quantization magnetic field in the z axis for the following state preparation and Raman interrogation stages. The atoms are prepared in the $F = 1$, $m_F = 0$ state in three steps with use of the lasers from the vertical beam path. First, a 60- μ s pulse of $F = 2 \rightarrow F' = 2$ transition light pumps the atoms to the $F = 1$ state. Second, a 30- μ s pulse of retroreflected σ^+ - and σ^- -polarized $F = 1 \rightarrow F' = 0$ light pumps the atoms to the $m_F = 0$ sublevel. Third, a 40- μ s pulse of $F = 2 \rightarrow F' = 3$ light removes the atoms left in the $F = 2$ state. The final population in the $F = 1$, $m_F = 0$ state is at least 85%.

After state preparation, we apply Raman pulses with $T = 8$ ms and π -pulse time $t_\pi = 4.4$ μ s. The Raman-laser frequencies are tuned 695.815 MHz below the $F' = 3$ level in the $5P$ manifold of hyperfine states. The maximum separation of the wave packets is about 94 μ m, and the enclosed Sagnac area, calculated with the root-mean-square velocity of the atoms, is about 0.03 mm². We delay the Raman-laser pulse sequence until 8 ms after the end of the molasses stage so that the desired Doppler-sensitive and magnetically insensitive Raman transitions are well resolved from unwanted Raman transitions (which are excited due to the finite polarization extinction ratio and/or spurious reflections of the Raman beams). The power in each Raman-laser beam is adjusted to minimize the ac Stark shift of the Raman transition frequency. The cold-atom cloud falls about 3 mm in each experimental cycle.

The rotation fringes are imprinted in both ⁸⁷Rb hyperfine ground states and the patterns are complementary to each other. Detecting either state is sufficient and the population

ratio is not required, but detecting both states would increase the signal-to-noise ratio if the difference in the Gaussian cloud shapes, due to imaging delays or optical pushing, could be balanced. In our case, the initial state of the atoms is $F = 1$, $m_F = 0$, and for technical reasons only the atoms transferred to the $F = 2$ state after the Raman pulse sequence are imaged. We take an absorption image of the atoms in the $F = 2$ state with a $5\text{-}\mu\text{s}$ pulse of $F = 2 \rightarrow F' = 3$ probe-laser light, pump the atoms to the $F = 1$ non-imaged state with 2 ms of the MOT cooling light, and then take an image of the probe-laser light field. From those two images, the density of the final cloud in the $F = 2$ state integrated along the z axis is calculated. Typically, there are 2×10^6 atoms in the $F = 2$ state at detection.

IV. ROTATION-FRINGE DETECTION

We characterize the PSI gyroscope with simulated rotations by tilting the retroreflecting mirror in Fig. 2 during the Raman interrogation, which is formally equivalent to rotating the entire system [40]. The mirror is mounted on a piezoactuated platform, whose x and y angular displacements are controlled by analog voltages. The simulated rotation is about 10^3 times larger than Earth's rotation and generates about one fringe period across the final cloud.

In our setup, the direction of the Raman-laser beams is in the direction of the local gravity vector \mathbf{g} , so the frequency difference between the Raman lasers is chirped to compensate for the Doppler shift due to the free fall of the atoms. With this frequency chirp, the acceleration phase is $(k_{\text{eff}}\mathbf{g} - 2\pi\alpha)T^2$ [41], where α is the chirp rate. As a consequence, scanning the chirp rate α provides a convenient way to scan the acceleration phase.

We detect the rotation-fringe images from the raw absorption images with principal component analysis (PCA) [42,43]. PCA has been widely used in machine learning. A few examples of PCA applications in cold-atom physics can be found in Refs. [36,43–45]. In our case, PCA can be considered an imaging analogy of lock-in detection. We scan the acceleration phase by scanning the chirp rate α so that the rotation fringes translate from shot to shot. The PCA algorithm identifies the moving components such as the rotation fringes from the raw images.

To use PCA in our experiment, we record a series of images at different chirp rates. The images are averaged to create a mean image in which the moving fringes are washed out but the envelope of the cold-atom cloud is retained. The mean image is then subtracted from each image to create a set of zero-mean images. These zero-mean images are the input to the PCA algorithm, which returns two main outputs: (i) a set of basis images called ‘‘principal components’’ (PCs) and (ii) the variance for each PC, which is the variance of the projection of each input image onto that PC. We adapted the computer code

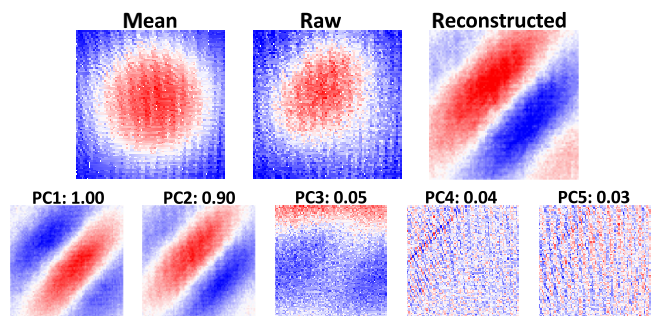


FIG. 3. PCA example for a set of 201 raw absorption images. Images are autoscaled, with red indicating the $F = 2$ population maxima and blue indicating the minima. The top row shows the mean image, the first image of the data set, and the first image reconstructed with only PC1 and PC2 (mean image subtracted). Because of the Gaussian cloud shape and other noise in the image, it is difficult both to see the rotation fringes in the raw image and to do a two-dimensional fit to the fringes. The bottom row shows the first five PCs and their variances. The variances are normalized to the value of PC1. All images have the same physical size, $2.1 \times 2.1 \text{ mm}^2$, and the same number of pixels, 80×80 . The simulated rotation is $2.94^\circ/\text{s}$ in the diagonal direction. The average of the rotation rates measured from the reconstructed images is $2.70^\circ/\text{s}$, which is lower than the applied rate because of the finite size of the initial cloud [39]. The rotation fringe contrast is about 50% after we process the images with PCA.

provided in the appendix in Ref. [42] to compute the outputs of PCA through singular-value decomposition. Figure 3 shows an example of PCA. Because the rotation fringes move as we scan the acceleration phase, the PCA returns a pair of principal components, PC1 and PC2, that have the same period and orientation as the rotation fringes but are 90° out of phase (sinelike and cosinelike). The linear combination of PC1 and PC2, with their projections onto each raw image varying from frame to frame, recreates the moving fringes; as a result, they have the highest variances of the projections. The other PCs, for example, the thin stripes caused by our imaging system (PC4 and PC5), do not follow the scanning of the acceleration phase; they are relatively static in the images and have smaller variances. In general, features of interest can be enhanced by reconstructing the images using only the PCs with the largest variances when we intentionally perturb the system, such as by scanning the acceleration phase.

We reconstruct the fringe images with only the sinelike and cosinelike PCs and disregard all the other PCs of lower variances. The reconstructed and zero-mean images are two-dimensionally fitted with $n(x, y) = A \exp(-x^2/2\sigma_x^2 - y^2/2\sigma_y^2) \cos(k_x x + k_y y + \phi)$, where A , σ_x , σ_y , k_x , k_y , and ϕ are fit coefficients. We call ϕ the offset phase of the rotation fringes. The components of rotation in the x and y directions are calculated as $\Omega_x = k_y T_{\text{ex}}/2k_{\text{eff}}T^2$ and $\Omega_y = -k_x T_{\text{ex}}/2k_{\text{eff}}T^2$. The rotation rate is $\sqrt{(\Omega_x^2 + \Omega_y^2)}$ and the rotation direction is $\tan^{-1}(\Omega_y/\Omega_x)$.

V. ACCELERATION AND ROTATION WITH PSI

As shown in Fig. 3, one can tell by inspecting the orientation of the fringes that the projection of the rotation vector onto the x - y plane points to 45° with respect to the image axis. However, the fringes induced by clockwise or counterclockwise rotations appear parallel in their respective images. The clockwise and counterclockwise rotations are distinguished by our scanning the acceleration phase and observing in which direction the fringes translate. The rotation fringes propagate like a plane wave traveling in the cold-atom cloud when the acceleration phase increases or decreases. The population ratio varies as $\cos[\mathbf{k}_\Omega \cdot \mathbf{r} - (2\pi T^2)\alpha + \phi_0]$, where α is the Raman-laser chirp rate and ϕ_0 is the phase due to the Raman lasers and a homogeneous acceleration. Because the phase gradients generated by opposite rotations have opposite sign, the rotation fringes move in opposite directions when we scan the acceleration phase by scanning the chirp rate.

When the rotation is large enough to generate one fringe across the cloud, the translational movement of the rotation fringes gives a measurement of the acceleration. Figure 4 shows a plot of the offset phase extracted from the two-dimensional fits as a function of the chirp rate. In this plot of the offset phase versus the chirp rate, we fit the data with a line and keep the slope as a fixed parameter with the value of $-2\pi T^2$, where $T = 8$ ms. The sensitivity of the acceleration measurement is calculated from the acceleration-phase fluctuations, $\delta\Phi$, with $\delta g/g = \delta\Phi/(gk_{\text{eff}}T^2)$ [46,47].

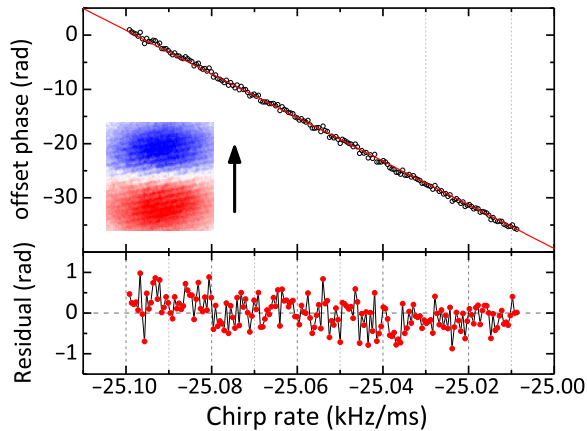


FIG. 4. Offset phase of the rotation fringes as the acceleration phase is scanned by scanning the Raman-laser chirp rate. The inset of a 2.1×2.1 mm² area shows the first fringe image (zero mean, reconstructed) in the data set of 181 images. The arrow indicates the direction of the fringes' travel. The red line is a linear fit with fixed slope -402.124 rad ms/kHz. The simulated rotation is $2.02^\circ/\text{s}$ in the $+x$ direction. The average measured rotation rate is $1.60^\circ/\text{s}$. The experimental repetition rate is 5 Hz and the duration of the data set is 36 s. The slow drift in the residual plot is likely due to the mechanism that generates the chirp, which is explained in Appendix A.

In our case, we interpret the root-mean-square of the residuals of the linear fit as $\delta\Phi$. In Fig. 4, $\delta\Phi$ is 0.369 rad with 0.2 s between data points, corresponding to a fractional acceleration sensitivity $\delta g/g$ of $1.6 \times 10^{-5}/\sqrt{\text{Hz}}$ when $T = 8$ ms. The sensitivity is currently limited by the Raman-laser phase noise and the vibration noise (see Appendix B).

VI. ROTATION-VECTOR SENSITIVITY

Figure 5 shows the Allan-deviation plots of the magnitude and the direction measurements of the rotation vector in the plane perpendicular to the direction of the Raman-laser beams from a data set with a data rate of 1 Hz and duration of 4000 s. For both quantities σ decreases as $\tau^{-1/2}$ from $\tau = 1$ s to $\tau = 10$ s. The intercept of the $\tau^{-1/2}$ -power-fit lines at $\tau = 1$ s gives an estimate of the sensitivity of measuring a rotation vector in the plane perpendicular to the Raman-laser beams: the sensitivity for the rate is $0.033^\circ/\text{s}$ and the sensitivity for the direction is 0.27° for an averaging time of 1 s.

In this data set, the experimental repetition rate is 10 Hz. In every 1 s, we record ten rotation-fringe images as the acceleration phase is scanned by 4 rad over the ten images while the chirp rate is scanned from -25.086 to -25.076 kHz/ms. We process the group of ten images with PCA and reconstruct these images with the sinelike and cosinelike PCs. All images are cropped to 1.8×1.8 mm² (70×70 pixels). By two-dimensionally fitting each reconstructed image, we obtain ten rotation rates and ten rotation directions. The average of the ten rotation rates (rotation directions) is used; as a result, we have a list of 4000 rotation rates (rotation directions) with a data rate of 1 Hz as the input for the Allan-deviation calculation.

The rotation measurements are based on the phase gradient in the cold-atom cloud, and since the laser phase noise and vibrations (parallel to \mathbf{k}_{eff}) create common-mode noise across the cloud that affects only the offset of the phase, the rotation sensitivity should be independent of those contributions to first order. The contributions to the noise in our rotation measurement are still under study. We estimate the contributions from the rotating mirror and the uncorrelated vibration of our floating optical table to be $2 \times 10^{-3}^\circ/\text{s}$ and $5 \times 10^{-5}^\circ/\text{s}$ for an averaging time of 1 s, respectively. The roll-off in Fig. 5 is likely due to a slow drift in the raw data. This could be produced, for example, through the voltage control of the piezoactuated platform that simulates the rotation, thermal effects, and/or the fluctuations in the cloud shape and size.

The average of the measured rotation rate is 92% of the simulated rotation rate in Fig. 3, 79% of that in Fig. 4, and 80% of that in Fig. 5 because of the finite size of the initial cloud [39]. The final cloud is 2.2 times bigger than the initial cloud in these measurement and we expect to see $1 - \sigma_0^2/\sigma_f^2 = 0.79$ of the simulated rotation assuming

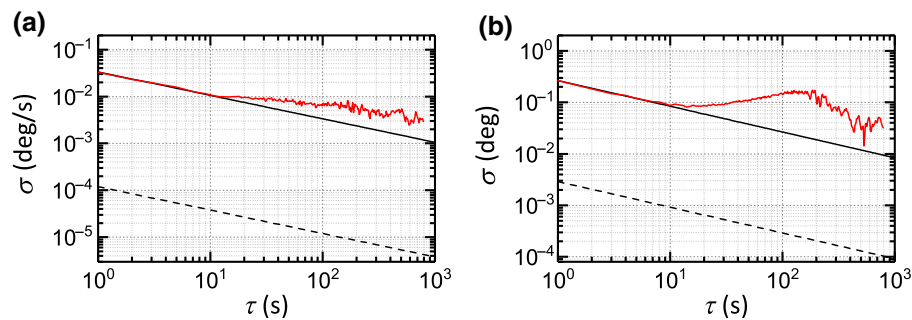


FIG. 5. The sensitivity of (a) the rate and (b) the direction of the rotation-vector measurement in the plane perpendicular to the direction of the Raman-laser beams. The solid black lines are $\tau^{-1/2}$ fits from $\tau = 1$ s to $\tau = 10$ s. The dashed black lines are the performances of an ideal point source limited by atom shot noise, estimated with total atom number 4×10^6 coherently interacting with the Raman interrogation lasers, image size 1.8×1.8 mm², $T = 8$ ms, and no dead time. The simulated rotation is $3.04^\circ/\text{s}$ in the $+x$ direction. The average of the measured rotation rate is $2.44^\circ/\text{s}$.

a Gaussian cloud shape. The discrepancy in the measurement could come from the Gaussian-shape approximation, fluctuations in cloud shape and size, and/or correlations between the position and velocity in the initial cloud when it is released from the MOT or molasses. Additional errors may arise from the calibration of the imaging system and the calibration of the simulated rotation.

VII. DISCUSSION

Wavefront aberration is one of the leading systematic errors in light-pulse atom interferometers [48,49]. In PSI this systematic error is expected to be larger because (i) the cloud necessarily expands and therefore samples more of the Raman-beam transverse profile and (ii) higher-order antisymmetric wavefront distortions will cause a phase gradient across the cloud and a corresponding systematic error in rotation. We estimate that the wavefront aberration due to the retroreflecting mirror that is specified for $\lambda/10$ flatness could create systematic errors in acceleration and rotation of up to $10^{-4}g$ and $0.07^\circ/\text{s}$, respectively.

The expansion of a cold-atom cloud smooths the structures that exist inside the cloud when it is released from the MOT and optical molasses. With a sufficiently large expansion factor, the expanding cloud becomes roughly Gaussian and the interferometer approaches the point-source limit. In the case when the expansion time is limited for high-bandwidth applications, we may optimize the cloud temperature so that the cloud expands faster for a given interrogation time, for example, by varying the cooling-laser detuning in the molasses stage. Fluctuations and variations in the initial cloud shape can and do cause noise and systematic shifts, however.

VIII. CONCLUSION AND OUTLOOK

By PSI, we demonstrate multiaxis inertial sensing: acceleration in the direction of the Raman-laser beams and

the projection of the rotation vector onto the plane perpendicular to that direction. The sensitivity of our present experiment is primarily constrained by the short Raman interrogation time ($T = 8$ ms), technical noise, the initial size of the cold-atom cloud, and the measurement dead time.

The finite initial size of the cold-atom cloud causes systematic errors in the rotation-vector measurement. In the case where the cloud expands by only a few times, the fluctuations in the cloud shape and size could affect the sensitivity of the rotation measurement. Stabilizing the cloud shape may allow us to control and to minimize such systematic errors. With a Gaussian cloud shape, the cloud width in the direction of the Raman-laser beams does not affect the rotation-vector measurement on the plane perpendicular to that direction; only the cloud shape in the plane does. We could use a one-dimensional optical lattice trap in the direction of the Raman-laser beams to initialize the cloud shape in the transverse direction. The density profile of the cloud released from a lattice trap relies on the profile and intensity of the lattice laser beam, which can be adjusted and feedback controlled.

The PSI instrument may be used very naturally as a gyrocompass [37]. In our experiment, the direction of the Raman-laser beams is parallel to \mathbf{g} and the cold-atom cloud is imaged in the plane normal to \mathbf{g} ; therefore, the atoms sense the projection of the rotation vector onto the plane tangent to the surface of Earth at the sensor location. The projection of Earth's rotation onto this plane points to geographic north. Hence, the direction of the rotation fringes due to Earth's rotation will point to geographic north and the number of the fringes will be proportional to the cosine of the latitude of the sensor location.

The PSI gyroscope is analogous to a mechanical gyroscope made of a spinning rotor. When the rotor spins about the z axis, it senses the projection of torque onto the x - y plane. In PSI, when the direction of the Raman-laser beams is along the z axis, the atoms sense the rotation projected

onto the x - y plane. The two-dimensional sensitivity of PSI may have applications in detecting time-varying rotation vectors, which is needed to measure a precession. In a simple case where the rotation vector traces a cone centered about the z axis, the precession can be measured by tracking the rotation component in the x - y plane.

ACKNOWLEDGMENTS

We thank Mark A. Kasevich, Rodolphe Boudot, and Moshe Shuker for helpful discussions. We thank James P. McGilligan for the comments on the manuscript. A.H. was supported for this work by an NRC Research Associateship award at NIST. This work was funded by NIST, a U.S. government agency, and it is not subject to copyright.

APPENDIX A: LASER SYSTEM

Figure 6 shows a schematic of our laser system, which provides the laser frequency components shown in Fig. 7. We use two commercially available 780-nm lasers. One is an external-cavity diode laser (ECDL) and the other is a frequency-doubled telecom laser that has a 20-kHz linewidth and output power up to 1 W. The ECDL, which is locked to a ^{87}Rb saturated absorption line via modulation-transfer spectroscopy [50], provides the MOT cooling

light. The telecom laser, locked to the ECDL via a heterodyne optical-phase-lock loop (OPLL) [51], provides the laser frequency components for all other frequencies in the experiment, including the repumper, state-preparation lasers, Raman lasers, and the probe laser. The OPLL allows us to switch the telecom-laser frequency over a range of several hundred megahertz in a few hundred microseconds.

For modulation-transfer spectroscopy, a double-pass acousto-optic modulator (AOM1 in Fig. 6) shifts the pump frequency by +160 MHz, so the Doppler-free spectral lines move by -80 MHz. The ECDL is locked to the redshifted crossover transition of $F = 2 \rightarrow F' = 2, 3$. The lock signal is generated by our modulating the frequency of the 80-MHz signal applied to AOM1 with a 250-kHz sine wave from the lock-in amplifier. The resulting frequency deviation is close to the half-linewidth of the saturated absorption resonance of ^{87}Rb . Such a choice maximizes the frequency-to-voltage conversion efficiency of the modulation-transfer spectrometer. Most of the ECDL power goes to another double-pass AOM in a cat's eye configuration [52] (AOM2 in Fig. 6) that shifts the laser frequency close to the cycling transition for use in the MOT. The light is red detuned from the cycling transition by 2.5Γ during the MOT phase and is linearly chirped to 14.4Γ during the molasses phase. The power of the cooling

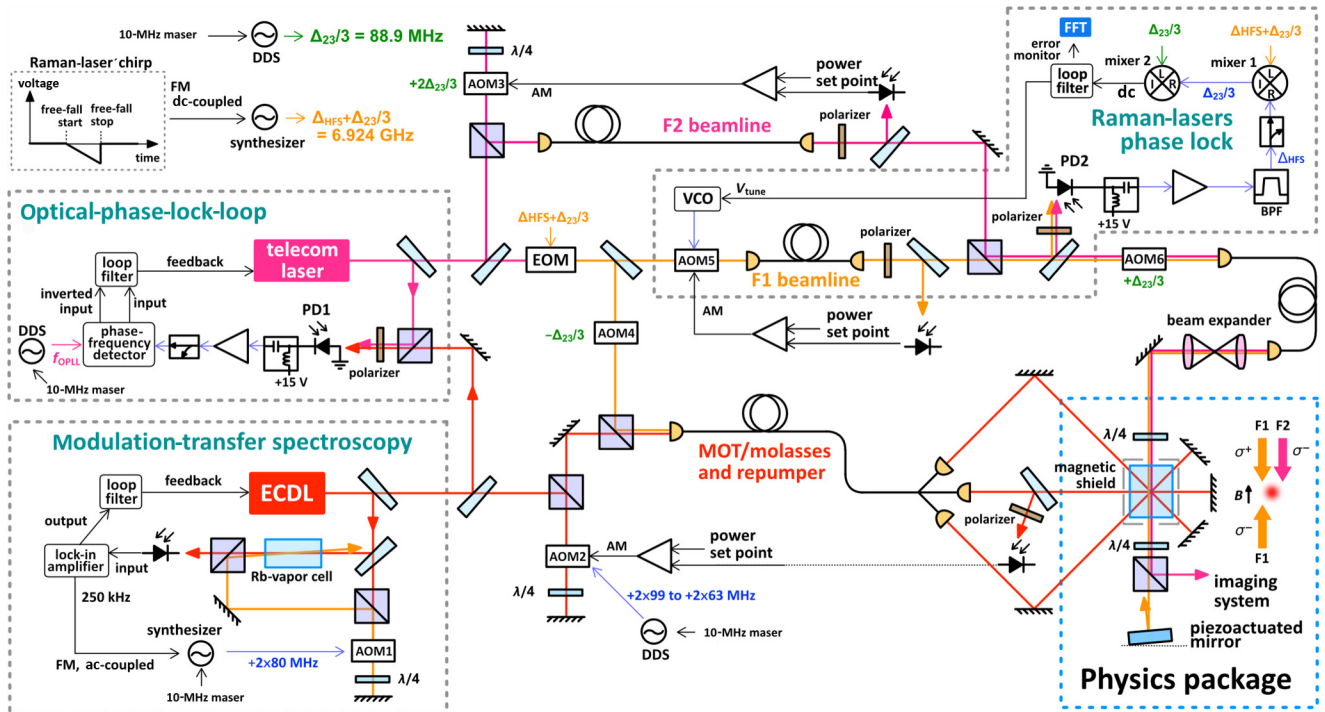


FIG. 6. Laser system. The ECDL is locked to a ^{87}Rb saturated absorption line. The telecom laser is locked to the ECDL by an OPLL. The set point f_{OPLL} cycles through four frequencies (as given in Fig. 7). With the use of the EOM and AOMs, the system provides all laser frequencies required in our experiment. The scanning of the Raman-laser chirp rate is done by our varying the slope of the triangular waveform applied to the dc-coupled frequency-modulation (FM) port of the synthesizer. AM, amplitude modulation; BPF, bandpass filter; DDS, direct digital synthesizer; PD, photodiode; VCO, voltage-controlled oscillator.

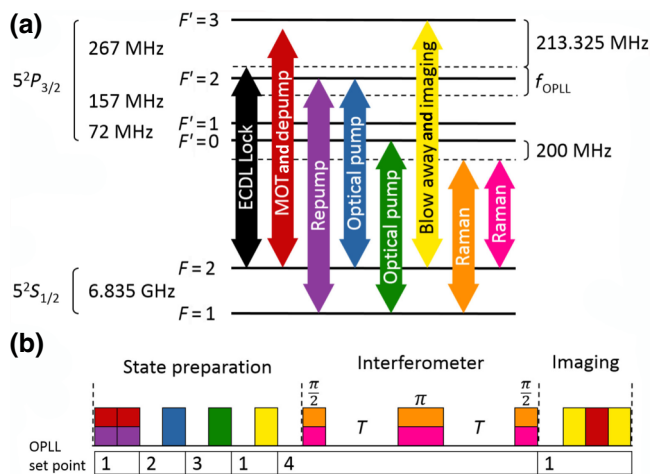


FIG. 7. Laser transition frequencies (a) and timing sequence (b). The black arrow shows the ECDL frequency when it is locked. The OPLL set point (f_{OPLL}) cycles through four frequencies: 53.325 MHz (1), 319.975 MHz (2), 549.140 MHz (3), and 749.140 MHz (4). The experimental repetition rate is 5 or 10 Hz. The energy levels and timing sequence are not to scale.

laser is actively stabilized and is linearly ramped down by a factor of 10 during the molasses phase.

A small portion of the ECDL light and the telecom-laser light is combined onto a fast photodiode (PD1 in Fig. 6) that measures the beat note between the two lasers. A digital phase-frequency detector compares the beat frequency with a stable rf reference (f_{OPLL}) and generates the OPLL lock signal. The telecom laser is phase-locked to the ECDL at a frequency that is below the lock point of the ECDL by f_{OPLL} (Fig. 7). The range of f_{OPLL} is limited by the maximal operating frequency of the digital phase-frequency detector (close to 1 GHz). The fractional power of the carrier in the beat note is greater than 99.73%, which corresponds to $2.7 \times 10^{-3} \text{ rad}^2$ in the residual phase fluctuation between the two lasers [51].

Most of the telecom-laser output is split into two beamlines, which we refer to as the “F1” and “F2” beamlines in Fig. 6. The F1 (F2) beamline is used for transitions starting from the $F = 1$ ($F = 2$) manifold. The F1 beamline contains an electro-optic phase modulator (EOM) that creates sidebands at $\Delta_{\text{HFS}} + \Delta_{23}/3 = 6.924 \text{ GHz}$, where $\Delta_{\text{HFS}} = 6.835 \text{ GHz}$ is the ground-state hyperfine-splitting frequency of ^{87}Rb and $\Delta_{23} = 266.650 \text{ MHz}$ is the difference between the $F' = 2$ and $F' = 3$ levels in the $5P$ states. The carrier is nulled by our tuning the rf power applied to the EOM. The F2 beam and the +1 sideband form the Raman beams. The combinations among the other sidebands and the F2 beam are off-resonant by multiples of $\Delta_{23}/3$.

Although both Raman beams are extracted from the same laser, their phase difference (i.e., the Raman-laser phase) fluctuates because of the physically different

F1-beam and F2-beam paths. The frequency of the voltage-controlled oscillator applied to AOM5 in the F1 beamline is feedback-controlled around 88.9 MHz to stabilize the phase difference of the two Raman beams. The dc lock signal is generated by our mixing down the beat note of the Raman beams with the two references: a microwave synthesizer, which drives the EOM and mixer 1, and a direct digital synthesizer that provides the common rf source $\Delta_{23}/3$ to AOM3, AOM4, AOM6, and mixer 2.

APPENDIX B: RAMAN-LASER PHASE NOISE

Figure 8 shows the power spectral densities of the major phase-noise sources present in our Raman lasers, including the residual Raman-laser phase noise and the absolute phase noise of the microwave synthesizer used as one of the two rf references in phase locking the Raman-laser beams. The residual Raman-laser phase noise, measured from the beat frequency of the Raman-laser beams when the phase lock is enabled, shows only the Raman-laser phase fluctuation relative to the rf references. The Raman phase noise that affects the atoms is the residual Raman-laser phase noise plus the phase noise of the rf references. However, in the low-frequency range ($1\text{--}10^4 \text{ Hz}$), which affects the interferometer phase the most, the contribution from the synthesizer dominates. Following the approach in Ref. [53], with $T = 8 \text{ ms}$, $t_\pi = 4.4 \mu\text{s}$, and an experimental repetition rate of 10 Hz, we estimate the instability of the interferometer phase arising from the Raman-laser phase noise (due to the microwave synthesizer) to be 90 mrad at 1 s. The corresponding instability of $\delta g/g$ at 1 s is 8.91×10^{-6} . In comparison, the phase instability due to the vibration (in the direction of the Raman lasers) of the mirror that retroreflects only the F1 beam is approximately 62 mrad at 1 s. The corresponding instability of $\delta g/g$ at 1 s

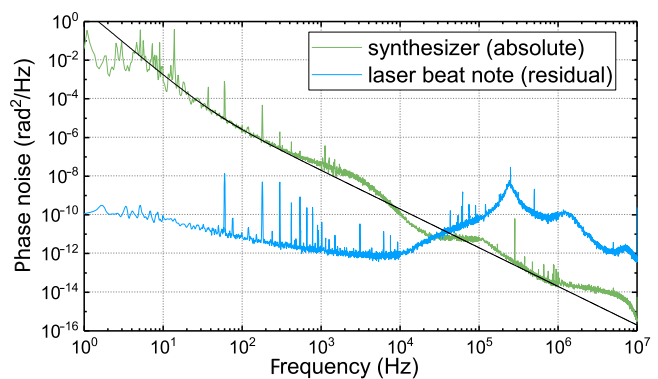


FIG. 8. Power spectral densities of the residual Raman-laser phase noise and the absolute phase noise of the synthesizer used as a reference in the Raman-laser phase lock. The spectra are taken when the dc-coupled frequency-modulation port of the synthesizer is enabled. The black line is the power fit $4/f^{3.4} + 0.02/f^2$ used in calculating the contribution from the synthesizer to the interferometer phase noise.

is 6.14×10^{-6} . The experiment is mounted on a floating optical table with no active vibration isolation.

-
- [1] S. Dimopoulos, P. W. Graham, J. M. Hogan, and M. A. Kasevich, Testing General Relativity with Atom Interferometry, *Phys. Rev. Lett.* **98**, 111102 (2007).
- [2] A. Arvanitaki, S. Dimopoulos, A. A. Geraci, J. Hogan, and M. Kasevich, How to Test Atom and Neutron Neutrality with Atom Interferometry, *Phys. Rev. Lett.* **100**, 120407 (2008).
- [3] P. W. Graham, J. M. Hogan, M. A. Kasevich, and S. Rajendran, New Method for Gravitational Wave Detection with Atomic Sensors, *Phys. Rev. Lett.* **110**, 171102 (2013).
- [4] B. Canuel *et al.*, Exploring gravity with the MIGA large scale atom interferometer, *Sci. Rep.* **8**, 14064 (2018).
- [5] A. Peters, K. Y. Chung, and S. Chu, Measurement of gravitational acceleration by dropping atoms, *Nature* **400**, 849 (1999).
- [6] G. Rosi, F. Sorrentino, L. Cacciapuoti, M. Prevedelli, and G. M. Tino, Precision measurement of the Newtonian gravitational constant using cold atoms, *Nature* **510**, 518 (2014).
- [7] P. Hamilton, M. Jaffé, P. Haslinger, Q. Simmons, H. Müller, and J. Khoury, Atom-interferometry constraints on dark energy, *Science* **349**, 849 (2015).
- [8] D. S. Durfee, Y. K. Shaham, and M. A. Kasevich, Long-Term Stability of an Area-Reversible Atom-Interferometer Sagnac Gyroscope, *Phys. Rev. Lett.* **97**, 240801 (2006).
- [9] B. Canuel, F. Leduc, D. Holleville, A. Gauguet, J. Fils, A. Viridis, A. Clairon, N. Dimarcq, C. J. Bordé, A. Landragin, and P. Bouyer, Six-Axis Inertial Sensor Using Cold-Atom Interferometry, *Phys. Rev. Lett.* **97**, 010402 (2006).
- [10] J. K. Stockton, K. Takase, and M. A. Kasevich, Absolute Geodetic Rotation Measurement Using Atom Interferometry, *Phys. Rev. Lett.* **107**, 133001 (2011).
- [11] I. Dutta, D. Savoie, B. Fang, B. Venon, C. L. Garrido Alzar, R. Geiger, and A. Landragin, Continuous Cold-Atom Inertial Sensor with 1 nrad/sec Rotation Stability, *Phys. Rev. Lett.* **116**, 183003 (2016).
- [12] D. Savoie, M. Altorio, B. Fang, L. A. Sidorenkov, R. Geiger, and A. Landragin, Interleaved atom interferometry for high-sensitivity inertial measurements, *Sci. Adv.* **4**, eaau7948 (2018).
- [13] R. Geiger, V. Ménotet, G. Stern, N. Zahzam, P. Cheinet, B. Battelier, A. Villing, F. Moron, M. Lours, Y. Bidel, A. Bresson, A. Landragin, and P. Bouyer, Detecting inertial effects with airborne matter-wave interferometry, *Nat. Commun.* **2**, 474 (2011).
- [14] B. Barrett, L. Antoni-Micollier, L. Chichet, B. Battelier, T. Lévêque, A. Landragin, and P. Bouyer, Dual matter-wave inertial sensors in weightlessness, *Nat. Commun.* **7**, 13786 (2016).
- [15] E. R. Elliott, M. C. Krutzik, J. R. Williams, R. J. Thompson, and D. C. Aveline, NASA's Cold Atom Lab (CAL): System development and ground test status, *npj Microgravity* **4**, 16 (2018).
- [16] D. Becker *et al.*, Space-borne Bose–Einstein condensation for precision interferometry, *Nature* **562**, 391 (2018).
- [17] P. Cheiney, L. Fouché, S. Templier, F. Napolitano, B. Battelier, P. Bouyer, and B. Barrett, Navigation-Compatible Hybrid Quantum Accelerometer Using a Kalman Filter, *Phys. Rev. Appl.* **10**, 034030 (2018).
- [18] Y. Bidel, O. Carraz, R. Charrière, M. Cadoret, N. Zahzam, and A. Bresson, Compact cold atom gravimeter for field applications, *Appl. Phys. Lett.* **102**, 144107 (2013).
- [19] T. Farah, C. Guerlin, A. Landragin, P. Bouyer, S. Gaffet, F. Pereira Dos Santos, and S. Merlet, Underground operation at best sensitivity of the mobile LNE-SYRTE cold atom gravimeter, *Gyroscopy Navigation* **5**, 266 (2014).
- [20] C. Freier, M. Hauth, V. Schkolnik, B. Leykauf, M. Schilling, H. Wziontek, H.-G. Scherneck, J. Müller, and A. Peters, Mobile quantum gravity sensor with unprecedented stability, *J. Phys.: Conf. Ser.* **723**, 012050 (2016).
- [21] Y. Bidel, N. Zahzam, C. Blanchard, A. Bonnin, M. Cadoret, A. Bresson, D. Rouxel, and M. F. Lequentrec-Lalancette, Absolute marine gravimetry with matter-wave interferometry, *Nat. Commun.* **9**, 627 (2018).
- [22] V. Ménotet, P. Vermeulen, N. Le Moigne, S. Bonvalot, P. Bouyer, A. Landragin, and B. Desruelle, Gravity measurements below 10^{-9} g with a transportable absolute quantum gravimeter, *Sci. Rep.* **8**, 12300 (2018).
- [23] T. L. Gustavson, P. Bouyer, and M. A. Kasevich, Precision Rotation Measurements with an Atom Interferometer Gyroscope, *Phys. Rev. Lett.* **78**, 2046 (1997).
- [24] T. L. Gustavson, P. Bouyer, and M. A. Kasevich, in Proc. SPIE (SPIE, 1998), Vol. 3270.
- [25] T. L. Gustavson, A. Landragin, and M. A. Kasevich, Rotation sensing with a dual atom-interferometer Sagnac gyroscope, *Classical Quant. Gravity* **17**, 2385 (2000).
- [26] T. Müller, M. Gilowski, M. Zaiser, P. Berg, C. Schubert, T. Wendrich, W. Ertmer, and E. M. Rasel, A compact dual atom interferometer gyroscope based on laser-cooled rubidium, *Eur. Phys. J. D* **53**, 273 (2009).
- [27] A. Gauguet, B. Canuel, T. Lévêque, W. Chaibi, and A. Landragin, Characterization and limits of a cold-atom Sagnac interferometer, *Phys. Rev. A* **80**, 063604 (2009).
- [28] G. Tackmann, P. Berg, C. Schubert, S. Abend, M. Gilowski, W. Ertmer, and E. M. Rasel, Self-alignment of a compact large-area atomic Sagnac interferometer, *New J. Phys.* **14**, 015002 (2012).
- [29] A. V. Rakholia, H. J. McGuinness, and G. W. Biedermann, Dual-Axis High-Data-Rate Atom Interferometer via Cold Ensemble Exchange, *Phys. Rev. Appl.* **2**, 054012 (2014).
- [30] P. Berg, S. Abend, G. Tackmann, C. Schubert, E. Giese, W. P. Schleich, F. A. Narducci, W. Ertmer, and E. M. Rasel, Composite-Light-Pulse Technique for High-Precision Atom Interferometry, *Phys. Rev. Lett.* **114**, 063002 (2015).
- [31] Z.-W. Yao, S.-B. Lu, R.-B. Li, J. Luo, J. Wang, and M.-S. Zhan, Calibration of atomic trajectories in a large-area dual-atom-interferometer gyroscope, *Phys. Rev. A* **97**, 013620 (2018).
- [32] M. Kasevich and S. Chu, Atomic Interferometry Using Stimulated Raman Transitions, *Phys. Rev. Lett.* **67**, 181 (1991).
- [33] X. Wu, F. Zi, J. Dudley, R. J. Bilotta, P. Canoza, and H. Müller, Multiaxis atom interferometry with a single-diode

- laser and a pyramidal magneto-optical trap, *Optica* **4**, 1545 (2017).
- [34] S. Wu, E. Su, and M. Prentiss, Demonstration of an Area-Enclosing Guided-Atom Interferometer for Rotation Sensing, *Phys. Rev. Lett.* **99**, 173201 (2007).
- [35] A. Tonyushkin and M. Prentiss, Straight macroscopic magnetic guide for cold atom interferometer, *J. Appl. Phys.* **108**, 094904 (2010).
- [36] S. M. Dickerson, J. M. Hogan, A. Sugarbaker, D. M. S. Johnson, and M. A. Kasevich, Multiaxis Inertial Sensing with Long-Time Point Source atom Interferometry, *Phys. Rev. Lett.* **111**, 083001 (2013).
- [37] A. Sugarbaker, S. M. Dickerson, J. M. Hogan, D. M. S. Johnson, and M. A. Kasevich, Enhanced Atom Interferometer Readout Through the Application of Phase Shear, *Phys. Rev. Lett.* **111**, 113002 (2013).
- [38] J. M. Hogan, D. M. S. Johnson, and M. A. Kasevich, in *Proceedings of the International School of Physics "Enrico Fermi": Atom Optics and Space Physics*, edited by E. Arimondo, W. Ertmer, W. P. Schleich, and E. M. Rasel (IOS Press, Amsterdam, 2009), p. 411.
- [39] G. W. Hoth, B. Pelle, S. Riedl, J. Kitching, and E. A. Donley, Point source atom interferometry with a cloud of finite size, *Appl. Phys. Lett.* **109**, 071113 (2016).
- [40] S.-Y. Lan, P.-C. Kuan, B. Estey, P. Haslinger, and H. Müller, Influence of the Coriolis Force in Atom Interferometry, *Phys. Rev. Lett.* **108**, 090402 (2012).
- [41] P. Cheinet, F. Pereira Dos Santos, T. Petelski, J. Le Gouët, J. Kim, K. Therkildsen, A. Clairon, and A. Landragin, Compact laser system for atom interferometry, *Appl. Phys. B* **84**, 643 (2006).
- [42] J. Shlens, A tutorial on principal component analysis, arXiv:1404.1100 (2014).
- [43] S. R. Segal, Q. Diot, E. A. Cornell, A. A. Zozulya, and D. Z. Anderson, Revealing buried information: Statistical processing techniques for ultracold-gas image analysis, *Phys. Rev. A* **81**, 053601 (2010).
- [44] R. Dubessy, C. D. Rossi, T. Badr, L. Longchambon, and H. Perrin, Imaging the collective excitations of an ultracold gas using statistical correlations, *New J. Phys.* **16**, 122001 (2014).
- [45] I. Ferrier-Barbut, M. Wenzel, M. Schmitt, F. Böttcher, and T. Pfau, Onset of a modulational instability in trapped dipolar Bose-Einstein condensates, *Phys. Rev. A* **97**, 011604(R) (2018).
- [46] T. Mazzoni, X. Zhang, R. Del Aguila, L. Salvi, N. Poli, and G. M. Tino, Large-momentum-transfer Bragg interferometer with strontium atoms, *Phys. Rev. A* **92**, 053619 (2015).
- [47] H. J. McGuinness, A. V. Rakholia, and G. W. Biedermann, High data-rate atom interferometer for measuring acceleration, *Appl. Phys. Lett.* **100**, 011106 (2012).
- [48] V. Schkolnik, B. Leykauf, M. Hauth, C. Freier, and A. Peters, The effect of wavefront aberrations in atom interferometry, *Appl. Phys. B* **120**, 311 (2015).
- [49] A. Trimeche, M. Langlois, S. Merlet, and F. Pereira Dos Santos, Active Control of Laser Wavefronts in Atom Interferometers, *Phys. Rev. Appl.* **7**, 034016 (2017).
- [50] M. Long-Sheng, L. Hollberg, J. H. Shirley, and J. L. Hall, US Patent No. 4,590,597 (1986).
- [51] D. Höckel, M. Scholz, and O. Benson, A robust phase-locked diode laser system for EIT experiments in cesium, *Appl. Phys. B* **94**, 429 (2008).
- [52] E. A. Donley, T. P. Heavner, F. Levi, M. O. Tataw, and S. R. Jefferts, Double-pass acousto-optic modulator system, *Rev. Sci. Instrum.* **76**, 063112 (2005).
- [53] P. Cheinet, B. Canuel, F. Pereira Dos Santos, A. Gauguier, F. Yver-Leduc, and A. Landragin, Measurement of the sensitivity function in a time-domain atomic interferometer, *IEEE Trans. Instrum. Meas.* **57**, 1141 (2008).